Nano Research

Open Access

Research Article

CeO_2-promoted spinel structural transformation enables CO_2 electroreduction to C_{2+} products

Yuan Chen, Shanshan Wu, Yue Zhai, Huizhi Li, Jiamin Zhu, Nan Zhang, Yuting Zhu, Zhuoyue Hou, Li An ✉, and Pinxian Xi ✉

State Key Laboratory of Natural Product Chemistry, Key Laboratory of Nonferrous Metal Chemistry and Resources Utilization of Gansu Province, Frontiers Science Center for Rare Isotopes, College of Chemistry and Chemical Engineering, Lanzhou University, Lanzhou 730000, China

Cite this article: *Nano Research*, **2025**, *18*, 94907898. https://doi.org/10.26599/NR.2025.94907898

ABSTRACT: Electrochemical CO_2 reduction reaction (CO_2RR) has received great attention in the past few decades as a promising process for reducing CO_2 emissions and producing high-value chemicals. However, the rational design of catalysts for CO_2RR continues to represent a significant challenge; hence, it is essential to understand the structure–property relationship and how catalysts facilitate CO_2 conversion. Herein, the tetrahedral site occupancy and octahedral site occupancy of spinel $CuAl_2O_4$ were modulated by constructing $CuAl_2O_4/CeO_2$ heterointerface, and the effect on CO_2RR performance was further investigated. In this work, we demonstrated that the octahedral site occupancy increases after constructing $CuAl_2O_4/CeO_2$ heterointerface, leading to a significant improvement in the catalyst's ability to absorb and activate CO_2 and enhance *CO coverage. Meanwhile, the unique oxyphilic property of CeO_2 enhances OH coverage and maintains the local pH on the catalyst surface. Ultimately, $CuAl_2O_4/CeO_2$ achieved 70.4% multi-carbon (C_{2+}) products Faraday efficiency (FE) in the flow cell and operated stably for over 35 h at a current density of 200 mA·cm^{-2} under 1 M KOH. $CuAl_2O_4/CeO_2$ exhibits completely different CO_2RR performance compared to pure $CuAl_2O_4$, providing new insights into accurate regulation of spinel structure.

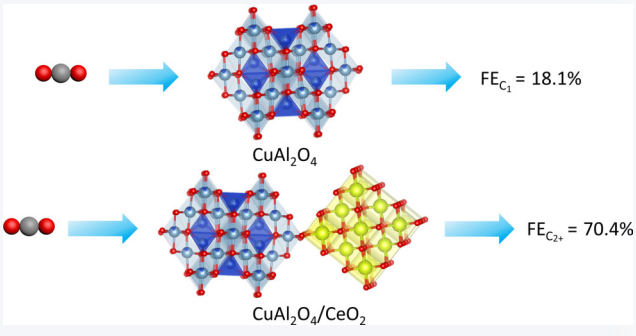

KEYWORDS: CO_2 reduction reaction (CO_2RR), spinel, heterointerface, CeO_2, structure modulation

1 Introduction

The excessive consumption of fossil fuels has led to elevated atmospheric CO_2 concentrations, resulting in global warming and climate change [1–4]. Consequently, the transformation of CO_2 into valuable chemicals and fuels through sustainable methodologies is imperative. Among these, CO_2 reduction reaction (CO_2RR) using renewable electricity shows promise, but faces challenges, such as high overpotentials, poor kinetics, and competing hydrogen evolution reaction (HER) [5, 6]. The research endeavor is centered on the design of efficient electrocatalysts, the optimization of conditions, and the elucidation of mechanisms to surmount these challenges.

Received: July 1, 2025; **Revised:** August 6, 2025
Accepted: August 6, 2025

✉Address correspondence to Li An, anli@lzu.edu.cn; Pinxian Xi, xipx@lzu.edu.cn

As an important class of transition metal compounds, spinel shows very attractive potential in a number of important electrochemical reactions, including oxygen evolution reaction (OER), HER, oxygen reduction reaction (ORR), etc. [7, 8]. The coexistence of tetrahedral (Td, A) and octahedral (Oct, B) sites in the spinel AB_2X_4 (X = O, S, Se, Te, N, etc.) structure has been demonstrated to accommodate different cations, thereby resulting in multiple possible geometrical configurations for cations [9–12]. In recent years, the optimization of spinel structure has emerged as a frontier research focus to address the persistent challenges in the catalytic performance of specific electrochemical reactions [13–15]. The main methods to modulate the structure of spinel include doping engineering, interfacial construction [16–20], and morphology modulation, to substantially enhance the catalytic performance of spinel.

As a key rare-earth oxide, CeO_2 has shown excellent potential for application in numerous catalytic reaction systems and has attracted extensive attention from researchers [20–22]. CeO_2

possesses unique electronic structure, with the 4f and 5d orbital electrons allowing for flexible switching of the Ce^{3+} and Ce^{4+}, and exhibits excellent performance in a variety of catalytic reactions due to its unique redox property and abundance of oxygen vacancies [23, 24]. Despite the extensive body of research on CeO_2-modified materials, the full potential of CeO_2 for catalyst structure modulation has yet to be fully realized.

Here, we report a strategy to modulate the geometrical configuration of spinel, which offers a novel solution to the poor performance in CO_2RR of the pure spinel by reasonably introducing CeO_2 in the $CuAl_2O_4$ catalyst. We used $CuAl_2O_4$ as a substrate to investigate the effect of modulating the geometrical configuration of spinel on its catalytic performance. It is generally recognized that Al is catalytically inactive in CO_2RR [25], thus leaving Cu as the only active metal in $CuAl_2O_4$. By changing the content of CeO_2, we screened the $CuAl_2O_4/CeO_2$ catalyst with the best performance. Experimental results suggest that the introduction of CeO_2 leads to an increase in the octahedral site occupancy of $CuAl_2O_4$, further promoting the adsorption of CO_2 and the coverage of *CO [26]. Simultaneously, CeO_2 itself also plays a positive role in the microenvironment of CO_2RR, localized alkalinity due to increased OH coverage further promotes C–C coupling.

2 Experimental section

2.1 Materials

Copper nitrate trihydrate ($Cu(NO_3)_3{\cdot}3H_2O$), aluminum nitrate nonahydrate ($Al(NO_3)_3{\cdot}9H_2O$), cerium(III) nitrate hexahydrate ($Ce(NO_3)_3{\cdot}6H_2O$), methanol (CH_3OH), anhydrous ethanol (CH_3CH_2OH), urea ($CO(NH_2)_2$), hexamethylenetetramine (HMT), polyvinylidene fluoride (PVDF), $KHCO_3$, and KOH were purchased from Aladdin. The commercial carbon paper was purchased from Fuel Cell Store. All the standard solutions were prepared with Milli-Q water with a resistance of 18 MΩ·cm.

2.2 Characterizations

X-ray diffraction (XRD) measurements were carried out on a Rigaku D/Max-2400 diffractometer with Cu Kα radiation (λ = 0.1542 nm) under a constant voltage of 40 kV. Transmission electron microscopy (TEM), high-resolution TEM (HRTEM) pictures, and energy dispersive spectroscopy (EDS) mapping of samples were obtained on a Tecnai G2 F30 field emission TEM. Atomic-scale scanning TEM (STEM) images were obtained using aberration-corrected STEM (Cubed Titan G2 60–300, FEI, USA) operated at 300 kV. X-ray absorption fine structure (XAFS) spectroscopy was carried out using the RapidXAFS 2M (Anhui Absorption Spectroscopy Analysis Instrument Co., Ltd.) by transmission (or fluorescence) mode at 20 kV and 20 mA, and the Si (553) spherically bent crystal analyzer with a radius of curvature of 500 mm was used for Cu. X-ray photoelectron spectroscopy (XPS) analysis was made with a Kratos Axis Supra device a VG ESCALAB 220I-XL device. All XPS spectra were corrected using C 1s line at 284.8 eV. Ultraviolet–visible (UV–vis) diffuse reflectance spectrum measurements were carried out on a Shimadzu UV-2600 spectrometer. Raman spectroscopy measurements were carried out on a LabRAM HR Evolution spectrophotometer with 532 nm wavelength of the excitation light source. *In situ* Raman measurements were experienced using the *in situ* electrochemical Raman cell (031-2H) with a saturated Ag/AgCl reference electrode and a Pt ring counter electrode by changing constant voltage in 0.1 M $KHCO_3$ to detect the surface chemical composition and structural evolution of materials. BRUKER-Fourier Transform Infrared (FTIR) Spectrometer-TENSOR27 was used. Attenuated total reflectance FTIR spectroscopy (ATR-FTIR) was investigated using a customized cell, with a saturated Ag/AgCl reference electrode and a Pt ring counter electrode in 0.1 M $KHCO_3$. *In situ* electrochemical characterization was carried out at specific potential for 10 min to obtain the surface chemical composition and structural information of materials.

Single-pulse ^{27}Al magic-angle spinning nuclear magnetic resonance (MAS NMR) spectra were recorded on a Bruker 600 MHz spectrometer at 130.33 MHz (11.7 T magnet) using a standard Bruker 2.5 mm MAS probe with a 30 kHz typical spinning frequency. The spectral width was set to 0.5 MHz, and the recycled time to D_0 = 5 s, long enough to avoid spin relaxation lattice constant (T_1) saturation effects. As ^{27}Al was a strong quadrupolar nucleus with spin quantum number (I) = 5/2, a short pulse length of 1.1 μs corresponding to a π/12 pulse determined using an aqueous 1 M $Al(NO_3)_3$ solution was employed. In these conditions, all the −1/2 → +1/2 central transitions were equally excited regardless of the magnitude of the nuclear quadrupole coupling constants, and one can extract quantitative data. The external reference was a 1 M $Al(NO_3)_3$ aqueous solution. For the samples containing only 4% of Al, overnight experiments (10,240 scans) were carried out to ensure a good signal/noise ratio.

2.3 Synthesis of $CuAl_2O_4$

2.0 mmol $Cu(NO_3)_3{\cdot}3H_2O$ and 4.0 mmol $Al(NO_3)_3{\cdot}9H_2O$ were dissolved in 20 mL CH_3OH and stirred to mix well. 10 mL CH_3OH containing 16.0 mmol $CO(NH_2)_2$ was slowly poured into the above solution and continued to stir for 30 min. The mixed solution was transferred to a 50 mL Teflon tank and reacted at 180 °C for 4 h. The collected precipitates were cleaned with deionized (DI) water and anhydrous ethanol, respectively, and then dried overnight in an oven at 60 °C. The obtained powder was calcined at 500 °C for 2 h in a Muff furnace with a heating rate of 10 °C·min^{-1} to obtain $CuAl_2O_4$ powder.

2.4 Synthesis of $CuAl_2O_4/CeO_2$

The as-prepared $CuAl_2O_4$ powder (1 mmol) was dispersed in 35 mL of absolute ethanol to form a suspension using ultrasonication. Then, 1 mmol of $Ce(NO_3)_3{\cdot}6H_2O$ and 3 mmol of HMT were added to the above solution. After that, the suspension was transferred to a 50 mL Teflon-lined stainless-steel autoclave and heated at 180 °C for 6 h. Finally, the gray powder was acquired by washing with DI water and absolute ethanol several times and drying at 60 °C in an oven under vacuum.

2.5 Preparation of the working electrode

10 milligrams of the electrocatalyst powder, 2 milligrams of PVDF, 2 milligrams of carbon black, and a certain amount of 1-methyl-2-pyrrolidone were mixed and ground for 10 min to obtain a homogeneous slurry. Subsequently, the slurry was transferred onto carbon paper and subjected to vacuum oven drying for a duration of approximately 12 h to yield the working electrode.

2.6 Electrochemical measurement

Electrochemical experiments were performed on a CHI 760E workstation in the H-type cell. The part of the cathode consists of a working electrode, reference electrode (saturated Ag/AgCl), and

CO_2-saturated 0.1 M $KHCO_3$; and the part of the anode consists of a counter electrode and 0.1 M $KHCO_3$. The following measurements were taken in order to ensure the accuracy of the results. First, the electrolyte (0.1 M $KHCO_3$) was bubbled with CO_2 for a minimum of 30 min. Then, CO_2 with a flow rate of 20 sccm was fed into the cathode electrolyte throughout the measurement.

2.7 Product analysis

The gaseous products from electrochemical CO_2RR were detected by online gas chromatography. The classification of the gaseous product was determined by measuring its retention time. The corresponding amounts of gaseous products were analyzed by the peak area. Specifically, a thermal conductivity detector (TCD) was utilized for the detection of H_2 and CO, while a flame ionization detector (FID) was employed for the detection of hydrocarbon products. The liquid products were collected subsequent to constant potential measurements and analyzed by ^{1}H NMR. Specifically, 0.1 mL of D_2O, including 0.05 μL of dimethyl sulfoxide (DMSO), was mixed with a 0.5 mL electrolyte.

2.8 Flow cell measurements

A three-electrode flow cell was used for electrocatalytic assessments. Ag/AgCl electrode (1 M KOH) served as the reference. Pt sheet was used as the counter electrode. All potentials were converted to the reversible hydrogen electrode (RHE) scale using the equation $E_{RHE} = E_{Ag/AgCl} + 0.197 + 0.059 \times pH$. Additionally, the anion exchange membrane was used to separate anode and cathode parts. The anode and cathode electrolytes were both composed of 1 M KOH, which were circulated by a peristaltic pump. The flow rates of CO_2 and the electrolyte are 20 and 60 mL·min^{-1}, respectively.

3 Results and discussion

3.1 Material synthesis and characterization

The synthesis of $CuAl_2O_4/CeO_2$ was accomplished through a two-step hydrothermal process, as outlined in the modified literature procedure. A series of characterizations was conducted for the purpose of identifying the structure and composition of $CuAl_2O_4$ and $CuAl_2O_4/CeO_2$. According to the results of powder XRD (Fig. 1(a)), the diffraction peaks at 31.3°, 36.8°, 59.4°, and 65.3° belong to the $CuAl_2O_4$ (PDF#71-967). In addition to the diffraction peaks of $CuAl_2O_4$, additional peaks at 28.5°, 33.1°, 47.4°, and 56.4° appeared in the pattern of $CuAl_2O_4/CeO_2$, which are attributed to the (111), (200), (220), and (311) facets of CeO_2 (PDF#43-1002), respectively. The XRD results confirmed the presence of both crystalline CeO_2 and $CuAl_2O_4$ in the $CuAl_2O_4/CeO_2$ catalysts. To further clarify the structure of catalysts, Raman spectroscopy was employed to conduct a meticulous analysis. The Raman peak at 465 cm^{-1} is attributed to the T_{2g} mode of CeO_2 with a fluorite structure (Fig. 1(b)), implying the successful introduction of CeO_2. Scanning electron microscopy (SEM) was used to characterize the morphology of the synthesized nanospheres. The presence of CeO_2-loading in $CuAl_2O_4$ nanospheres has been observed (Fig. S1 in the Electronic Supplementary Material (ESM)). Furthermore, HRTEM images show interplanar spacings of 0.269, 0.311, and 0.285 nm, assigned to the (200) and (111) planes of CeO_2 and the (220) plane of $CuAl_2O_4$, respectively (Fig. 1(c) and Fig. S2 in the ESM). Additionally, the fringes of $CuAl_2O_4$ and CeO_2 contact each other, indicating the formation of the heterointerface. As shown in Figs. 1(d)–1(f) and Fig. S3 in the ESM, the existence of two interfaces was clearly detected by high-angle annular dark-field STEM (HAADF-STEM) and mapping, which provides substantial evidence for the formation of heterointerface.

3.2 Electronic structure and geometrical configuration analysis

X-ray absorption spectroscopy (XAS) of the Cu K-edge was performed to understand the oxidation state and local microstructure of the Cu species. Figure 2(a) shows the normalized Cu K-edge X-ray absorption near-edge structure (XANES) spectra of $CuAl_2O_4/CeO_2$, $CuAl_2O_4$, and Cu foil. According to the edge

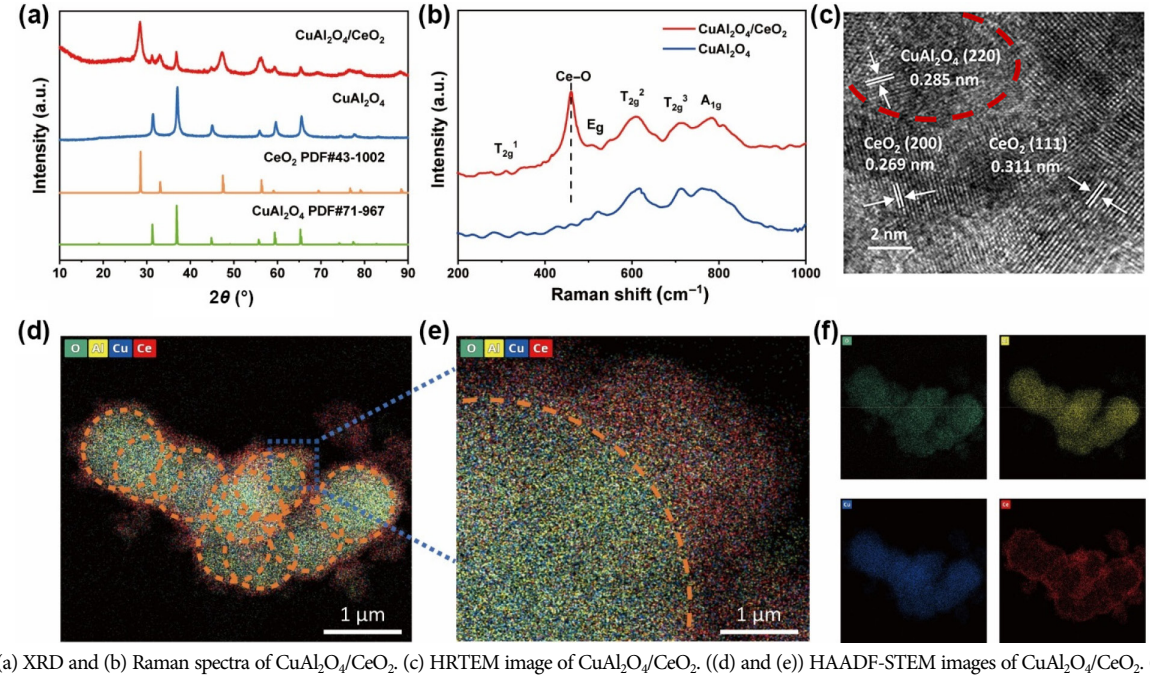

Figure 1 (a) XRD and (b) Raman spectra of $CuAl_2O_4/CeO_2$. (c) HRTEM image of $CuAl_2O_4/CeO_2$. ((d) and (e)) HAADF-STEM images of $CuAl_2O_4/CeO_2$. (f) Elemental mapping images of $CuAl_2O_4/CeO_2$.

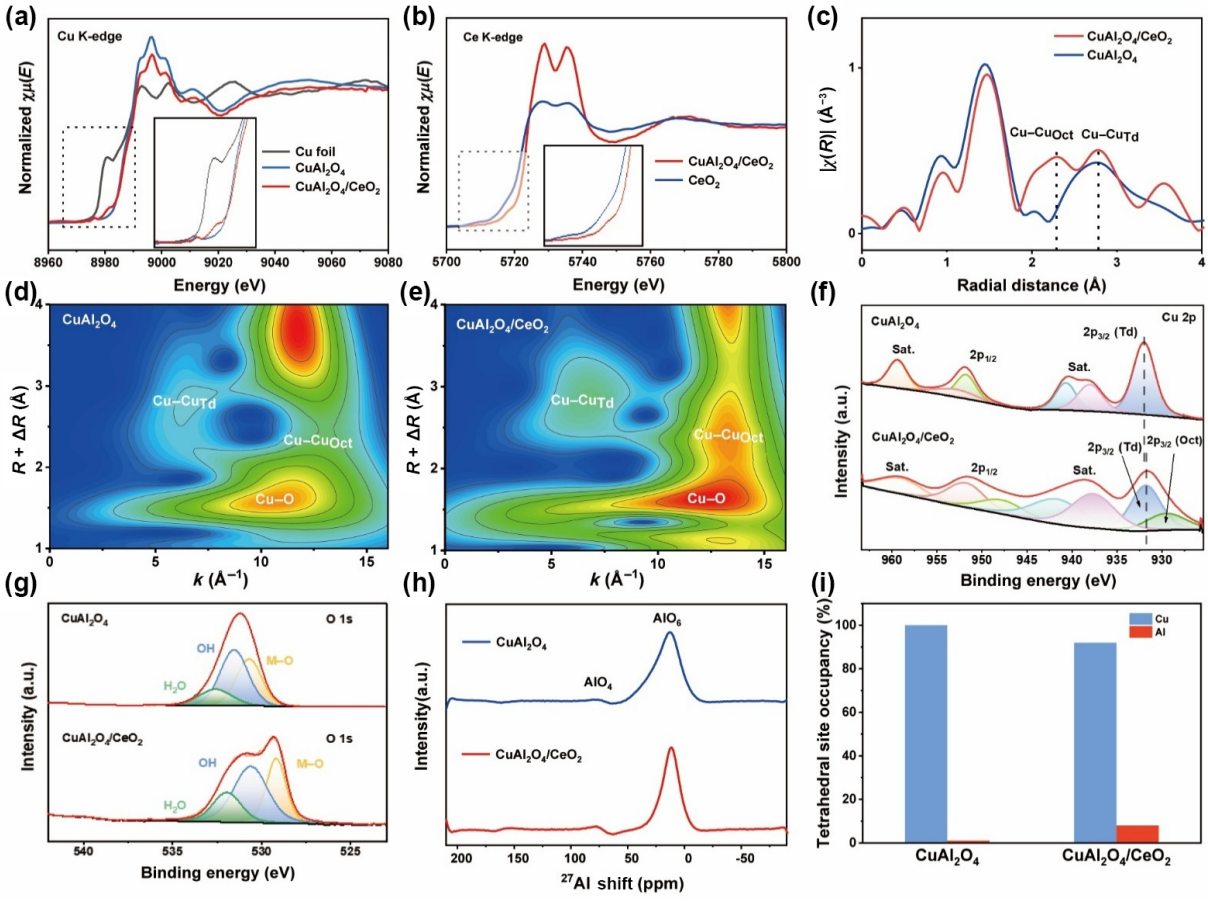

Figure 2 (a) Cu K-edge XANES spectra. (b) Ce K-edge XANES spectra. (c) FT of the Cu K-edge EXAFS spectra. ((d) and (e)) Wavelet transforms for the k^3-weighted EXAFS signals for $CuAl_2O_4$ and $CuAl_2O_4/CeO_2$. (f) Cu 2p XPS spectra of $CuAl_2O_4$ and $CuAl_2O_4/CeO_2$. (g) O 1s XPS spectra of $CuAl_2O_4$ and $CuAl_2O_4/CeO_2$. (h) ^{27}Al MAS NMR spectra of $CuAl_2O_4$ and $CuAl_2O_4/CeO_2$. (i) The tetrahedral site occupancy of $CuAl_2O_4/CeO_2$.

position, it infers that the electronic structure of Al changed after the introduction of CeO_2. The valence state of Cu on the surface decreases, which is conducive to generating active sites, such as Cu^+ and Cu^0. Similarly, according to Figs. 2(b) and Fig. 2(i), we confirmed the higher oxidation state of Ce in $CuAl_2O_4/CeO_2$ compared with the commercial CeO_2. The distribution of metal cations was determined through the implementation of extended XAFS (EXAFS), XPS, and ^{27}Al MAS NMR (Figs. 2(c)–2(f) and 2(h)) [27, 28]. The first large peak at around 1.5 in the EXAFS of Cu K-edge corresponds to the scattering of the nearest neighbor oxygen atoms, while the second large peak at around 2.8 arises from the scattering of the second nearest neighbor transition cations in both tetrahedral and octahedral sites. In contrast to $CuAl_2O_4$, the second large peak of the $CuAl_2O_4/CeO_2$ EXAFS spectra is split into two peaks, indicating the increase in octahedral site occupancy. In EXAFS wavelet transform (WT) analysis (Figs. 2(d) and 2(e)), substantial enhancement of the octahedral site signal relative to the tetrahedral site is also observed.

XPS measurements (Fig. 2(g) and Figs. S4 and S5 in the ESM) were further performed to probe the structural differences and variations in chemical environment [29]. Compared with that of $CuAl_2O_4$, the Cu 2p peak of $CuAl_2O_4/CeO_2$ shifted towards a lower binding energy, which indicated that Cu accepts electrons, thereby decreasing its valence state. Meanwhile, the Cu $2p_{3/2}$ peak of $CuAl_2O_4/CeO_2$ split into $2p_{3/2}$ (Td) and $2p_{3/2}$ (Oct), which is also strong evidence for increased octahedral site occupancy. The O 1s spectra show enhanced OH after the introduction of CeO_2, which is attributed to the unique redox property of CeO_2. In order to directly probe the environments of Al species in the $CuAl_2O_4$ and $CuAl_2O_4/CeO_2$ at a local scale, the ^{27}Al MAS NMR has been performed as a sophisticated method with atomic-level resolution [30]. Consistent with the ^{27}Al shifts that have been documented in the past for aluminum oxides, typical AlO_6 octahedra (15–25 ppm) and AlO_4 tetrahedra (65–85 ppm) aluminum environments have been observed for $CuAl_2O_4$ and $CuAl_2O_4/CeO_2$. We subsequently offer a concise synopsis of the tetrahedral site occupancy of $CuAl_2O_4$ and $CuAl_2O_4/CeO_2$ in the form of bar charts. The introduction of CeO_2 has been observed to result in a considerable augmentation of Al occupancy in the tetrahedral sites, escalating from nearly zero to 8.2%. Concurrently, the occupancy of Cu has been noted to undergo a decline, from 100% to 91.8% of the tetrahedral sites.

3.3 Electrochemical CO_2RR performance

The electrochemical CO_2RR performance was evaluated by electrolysis at a specific current density in a flow-cell reactor. All potentials were referenced to a RHE without *iR* compensation. The linear scanning voltammetry (LSV) curves of $CuAl_2O_4/CeO_2$ under CO_2 and Ar flow atmospheres, respectively, were first tested in a flow cell of 1 M KOH (Fig. 3(a)).

The LSV showed that the activity of $CuAl_2O_4/CeO_2$ in CO_2 was higher than that in Ar, with a lower onset potential and a higher

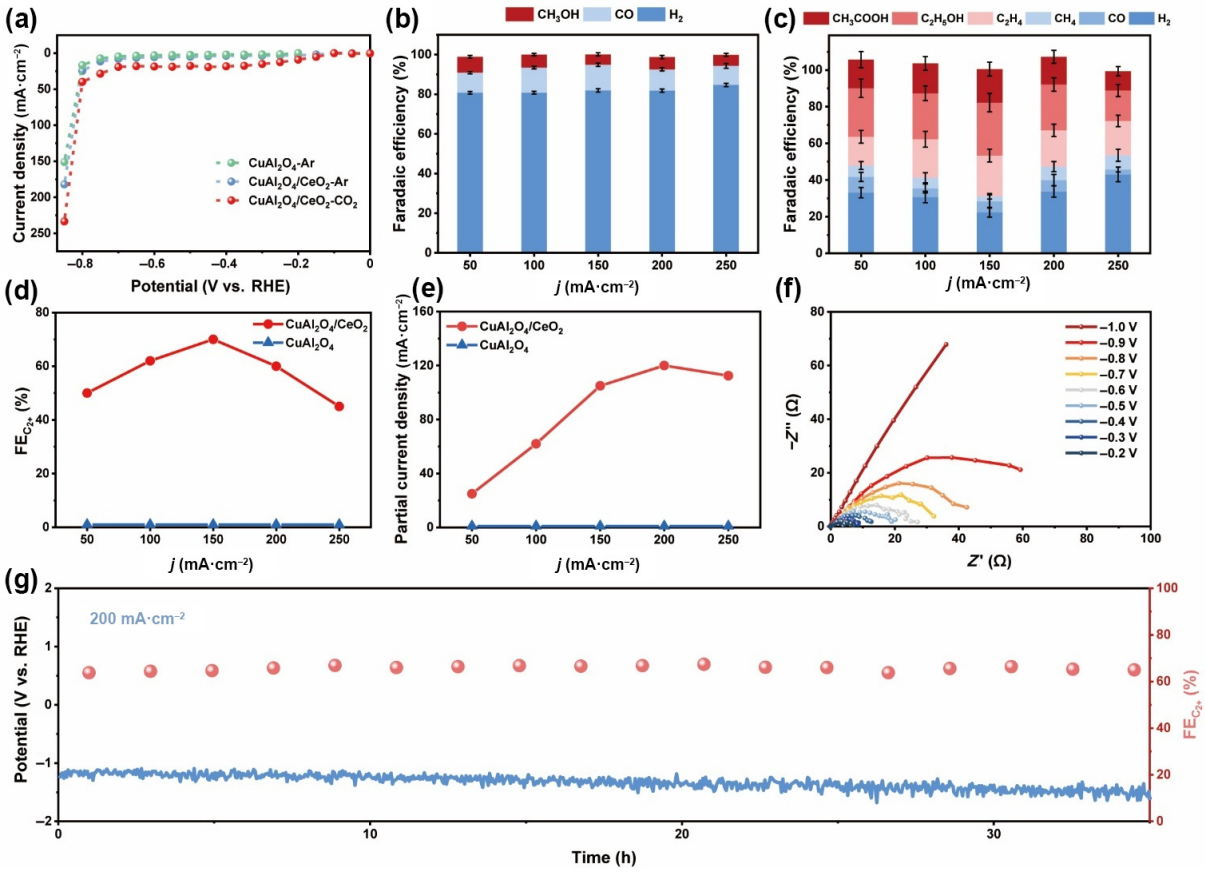

Figure 3 (a) LSV curves in 1 M KOH electrolyte. ((b) and (c)) FE values of each CO_2RR product and H_2 on (b) $CuAl_2O_4$ and (c) $CuAl_2O_4/CeO_2$ at different current densities in 1 M KOH. (d) FE values and (e) partial current densities of C_{2+} products on $CuAl_2O_4$ and $CuAl_2O_4/CeO_2$. (f) Nyquist plots of $CuAl_2O_4$ and $CuAl_2O_4/CeO_2$. (g) Stability performance of $CuAl_2O_4$ to produce C_{2+} products.

current density. In addition, under the Ar flow atmosphere, the current density of $CuAl_2O_4/CeO_2$ is higher than that of $CuAl_2O_4$, indicating that $CuAl_2O_4/CeO_2$ demonstrates superior electrical conductivity relative to $CuAl_2O_4$. The electrical conductivity of the catalysts was further investigated by UV–vis diffuse reflectance spectroscopy (UV–vis DRS) and bandgap (E_g) (Fig. S6 in the ESM). After the introduction of CeO_2, the E_g of the catalyst is reduced from 2.9 to 2.7 eV. The narrowing of E_g promotes the transfer of electrons, leading to an increase in electrical conductivity. Subsequently, the CO_2RR performance of $CuAl_2O_4$ and $CuAl_2O_4/CeO_2$ was systematically evaluated at different current densities in the flow cell (Figs. 3(b)–3(e) and Figs. S8 and S9 in the ESM). The Faraday efficiency for C_{2+} products ($FE_{C_{2+}}$) values show a volcano-shaped profile in the current density range of 50–250 mA·cm^{-2}. *In situ* electrochemical impedance spectroscopy (EIS) was adopted to assess reaction kinetics (Fig. 3(f) and Fig. S7 in the ESM). We have tested the electrochemical impedance of $CuAl_2O_4$ and $CuAl_2O_4/CeO_2$ under conditions ranging from −0.2 to −1.0 V. The impedance semicircle of $CuAl_2O_4/CeO_2$ was smaller, indicating that $CuAl_2O_4/CeO_2$ has a faster charge transfer rate. At 150 mA·cm^{-2}, the $FE_{C_{2+}}$ of $CuAl_2O_4/CeO_2$ reached the highest value of 70.4%, corresponding to a partial current density of 105 mA·cm^{-2} for C_{2+} ($j_{C_{2+}}$ = 105 mA·cm^{-2}). In contrast, $CuAl_2O_4$ only exhibited activity towards C_1 production, including CO and CH_3OH, in the tested current density range. The high $FE_{C_{2+}}$ of $CuAl_2O_4/CeO_2$ indicates that *CO is moderately adsorbed on the surface, which facilitates C–C coupling rather than easy desorption. At 200 mA·cm^{-2}, the C_{2+} partial current density of $CuAl_2O_4/CeO_2$ reached its highest value ($j_{C_{2+}}$ = 145 mA·cm^{-2}). Concurrently, the C_{2+} partial current density of $CuAl_2O_4$ was nearly zero, which indicates that the ability to promote C–C coupling is not present in $CuAl_2O_4$. The CO_2RR stability of $CuAl_2O_4/CeO_2$ was assessed in the flow cell of 1 M KOH under CO_2 atmosphere. It is generally believed that the gas diffusion layer suffers from losing hydrophobicity and being flooded over time. Therefore, the gas diffusion layer was modified with polytetrafluoroethylene (PTFE) to prevent salt accumulation. The $FE_{C_{2+}}$ value showed a marginal reduction (< 5%) during an operation period of 35 h at 200 mA·cm^{-2} (Fig. 3(g)).

3.4 Investigation of reaction mechanism

In order to evaluate the adsorption capacity of catalysts for CO_2 and reaction intermediates, temperature programmed desorption of CO_2 (CO_2-TPD) and the electrochemical quartz crystal microbalance (EQCM) were used to characterize the catalysts (Figs. 4(a)–4(c)). CO_2-TPD of $CuAl_2O_4$ shows two desorption peaks, which are centered at 110 and 400 °C. While CO_2-TPD of $CuAl_2O_4/CeO_2$ shows three desorption peaks, which are centered at 110, 460, and 560 °C, the occurrence of a peak at 560 °C is attributed to the process of CO_2 adsorption by CeO_2. After the introduction of CeO_2, the signal intensity of CO_2 adsorption dramatically increased in most temperature intervals, demonstrating the enhanced CO_2 adsorption capacity of the catalysts. According to the results of EQCM, at the initial application of voltage, $CuAl_2O_4$ experienced a mass increase

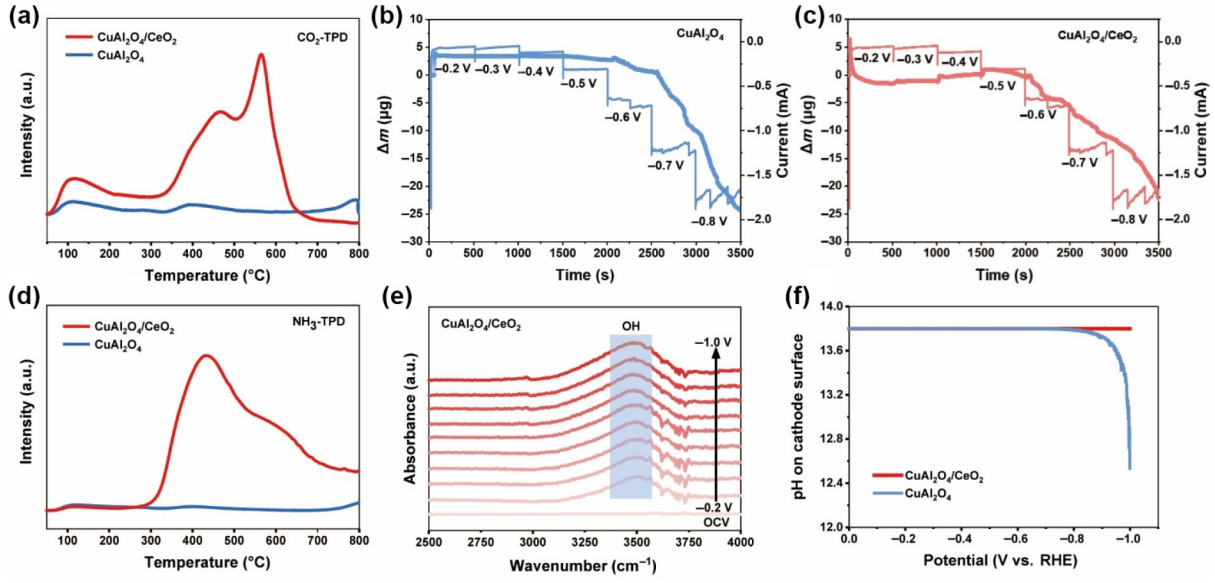

Figure 4 (a) CO_2 TPD curves of $CuAl_2O_4$ and $CuAl_2O_4/CeO_2$. ((b) and (c)) Mass change of (b) $CuAl_2O_4$ and (c) $CuAl_2O_4/CeO_2$ with potential. (d) NH_3 TPD curves of $CuAl_2O_4$ and $CuAl_2O_4/CeO_2$. (e) *In situ* ATR-FTIR spectra of $CuAl_2O_4/CeO_2$. (f) The pH changes on the $CuAl_2O_4$ and $CuAl_2O_4/CeO_2$ surface varies with voltage.

of 4.1 μg, while $CuAl_2O_4/CeO_2$ experienced a mass increase of 6.9 μg. This is also strong evidence for the enhanced adsorption capacity of the catalyst for CO_2. Meanwhile, the multi-step potential measurements revealed that the total mass of catalysts decreased due to structural reconstruction under the application of negative potentials. Compared with $CuAl_2O_4$, $CuAl_2O_4/CeO_2$ exhibited lower mass variation; this observation suggests that the interface structure plays a pivotal role in mitigating catalyst reconstruction. To investigate the microenvironment of the catalyst during the reaction process, the Lewis acidity of the catalysts was first characterized by NH_3-TPD. As illustrated in Fig. 4(d), the adsorption capacity of $CuAl_2O_4$ and $CuAl_2O_4/CeO_2$ for NH_3 varies with temperature, with higher peak intensities implying higher Lewis acidity. The latest research shows that a Lewis acid layer can be introduced over transition metal oxide catalysts to dynamically decompose water molecules and capture hydroxyl anions. Compared to $CuAl_2O_4$, $CuAl_2O_4/CeO_2$ exhibits increased Lewis acidity, indicating stronger ability to attract OH. *In situ* ATR-FTIR spectra show that the intensity of the OH peak increases in proportion to the applied voltage (Fig. 4(e)), and the maintenance of local alkalinity was further demonstrated by local pH measurement on IrO_x-modified rotating ring-disk electrode (RRDE) (Fig. 4(f) and Fig. S10 in the ESM). As the applied voltage increases from −0.2 to −1.0 V, the OH coverage on the surface of $CuAl_2O_4/CeO_2$ continues to increase, while the local pH remains almost unchanged. Conversely, $CuAl_2O_4$ exhibits localized alkalinity weakening with increasing voltage.

The catalyst after the stability test was characterized by XRD, SEM, and EDS. Interestingly, as indicated by the XRD spectra after CO_2RR (Fig. 5(a)), the phase of the catalyst remained constant. However, the peak intensity underwent a reduction, particularly in the case of CeO_2. We suggest that CeO_2 maintains the structure and components of catalysts through its redox capacity; this conclusion was corroborated by *in situ* Raman spectroscopy (Figs. 5(b)–5(d)). According to the results of SEM and EDS before and after CO_2RR (Figs. S9 and S10 in the ESM), after conducting stability test, catalysts surface roughening was observed, which was accompanied by an increase in Cu and Al atom content, as well as a decrease in Ce and O atom content, indicating an increase in the active sites. Raman peak intensities of 462, 620, 722, and 776 cm^{-1} in $CuAl_2O_4$ and $CuAl_2O_4/CeO_2$ were also extracted. Discovered by *in situ* Raman spectra, the T_{2g} peak intensity of CeO_2 decreased significantly with increasing applied voltage. Meanwhile, the T_{2g}^2, T_{2g}^3, and A_{1g} peak intensity of $CuAl_2O_4$ decreased by a small margin proportionally. Therefore, it can be concluded that CeO_2 is more unstable during CO_2RR, or CeO_2 plays a role in inhibiting structural reconstruction and stabilizing $CuAl_2O_4$. *In situ* monitoring of intermediates is conducive to analyzing the catalytic reaction process and guiding the design and synthesis of excellent catalysts. Therefore, the mechanism of the catalytic reaction was further elucidated by *in situ* ATR-FTIR spectroscopy and the extracted peak intensity of *in situ* ATR-FTIR spectroscopy (Figs. 5(e)–5(i)). With the negative shift in potential, *in situ* ATR-FTIR spectroscopy of $CuAl_2O_4/CeO_2$ shows an absorption peak near 2070 cm^{-1} that is attributed to *CO intermediate. We also observed the *OCCHO intermediate near 1140 cm^{-1}, which is the key intermediate of C_{2+} products and sign of successful C–C coupling. In contrast, we only observed *CHO near 1280 cm^{-1} and *COOH near 1430 cm^{-1}, which are both the key intermediates of C_1 products [31, 32]. *In situ* ATR-FTIR results show that the introduction of CeO_2 optimizes adsorption of *CO on the catalyst surface, and the coverage of *CO is significantly improved, thereby facilitating C–C coupling.

4 Conclusions

In this study, we demonstrated a strategy to modulate the tetrahedral and octahedral site occupancy of spinel $CuAl_2O_4$ by constructing a $CuAl_2O_4/CeO_2$ heterointerface, which significantly enhances CO_2RR performance. XAS, XPS, and ^{27}Al MAS NMR revealed that the introduction of CeO_2 leads to an increase in octahedral site occupancy of $CuAl_2O_4$, promoting the adsorption and activation of CO_2 and enhancing the surface coverage of *CO intermediates. Meanwhile, it was demonstrated that the unique oxyphilic property of CeO_2 enhances OH coverage and maintains local alkalinity on the catalyst surface to facilitate C–C coupling by *in situ* ATR-FTIR and local pH measurement. Finally, the $CuAl_2O_4/CeO_2$ catalyst achieves 70.4% $FE_{C_{2+}}$ in the flow cell and stably operates at a current density of 200 $mA{\cdot}cm^{-2}$ under 1 M KOH, exceeding 35 h, far surpassing pure $CuAl_2O_4$ with negligible

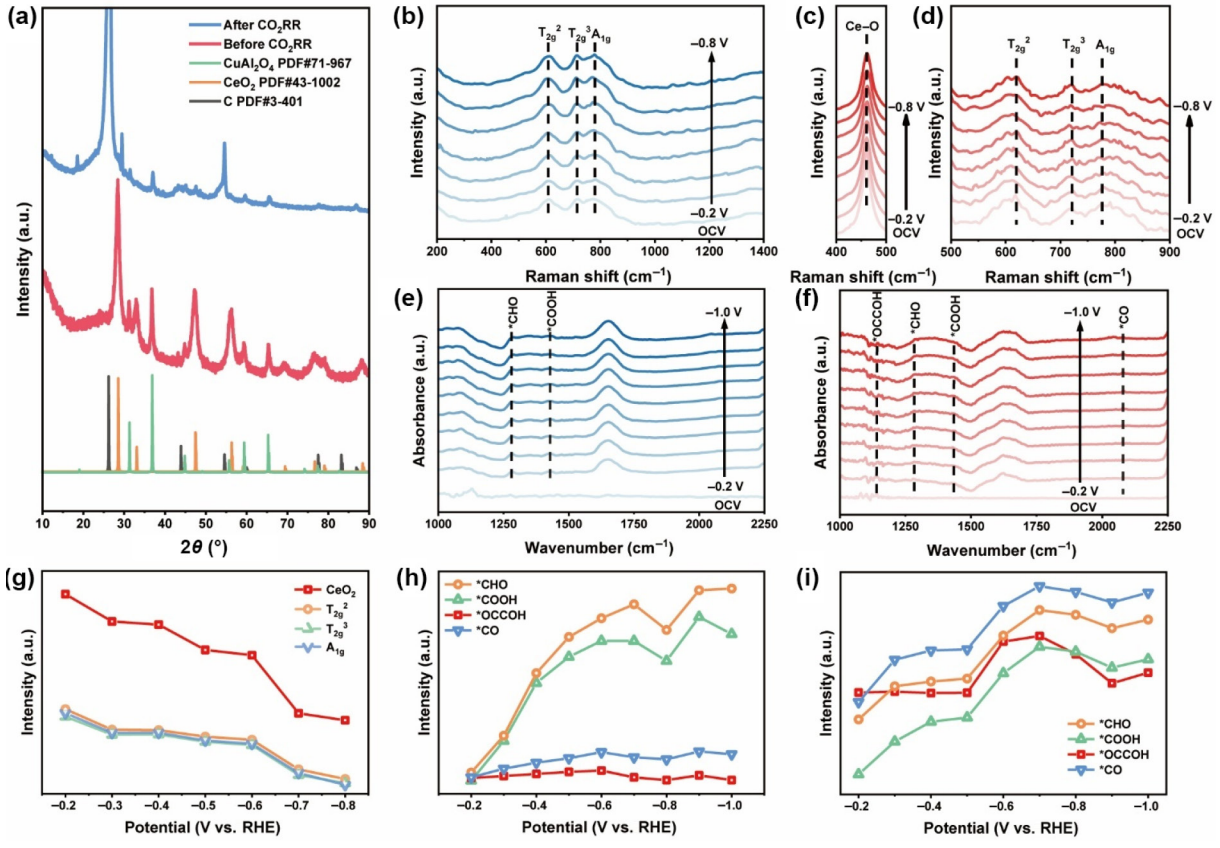

Figure 5 (a) XRD and spectra of $CuAl_2O_4$ and $CuAl_2O_4/CeO_2$ after CO_2RR tests. ((b)–(d)) *In situ* Raman spectra of $CuAl_2O_4$ and $CuAl_2O_4/CeO_2$. ((e) and (f)) *In situ* ATR-FTIR spectra of (e) $CuAl_2O_4$ and (f) $CuAl_2O_4/CeO_2$. (g) Extracted Raman peak in $CuAl_2O_4$ and $CuAl_2O_4/CeO_2$. ((h) and (i)) Extracted ATR-FTIR peak in (h) $CuAl_2O_4$ and (i) $CuAl_2O_4/CeO_2$.

C_{2+} production. This work provides new insights into precise regulation of spinel structures via heterointerface engineering, showing that modulating cation site occupancy and leveraging the oxyphilic property of CeO_2 are effective for enhancing CO_2RR activity and selectivity, paving the way for designing high-performance catalysts for sustainable CO_2 conversion.

Electronic Supplementary Material: Supplementary material (further details SEM, XPS, products analysis, and Raman spectroscopy measurements) is available in the online version of this article at https://doi.org/10.26599/NR.2025.94907898.

Data availability

All data needed to support the conclusions in the paper are presented in the manuscript and the Electronic Supplementary Material. Additional data related to this paper may be requested from the corresponding author upon request.

Acknowledgements

This work was funded by the National Key R&D Program of China (No. 2021YFA1501101), the National Natural Science Foundation of China (Nos. 22425105, 22221001, 22271124, 22471103, 22201111, and 22401120), and the 111 Project (No. B20027), as well as the Young Elite Scientists Sponsorship Program by Chinese Association for Science and Technology (CAST, No. 2023QNRC001). We also acknowledge support from the Science and Technology Major Plan of Gansu Province (Nos. 24ZD13GA015, 23ZDGA012, and 23ZDKA014) and the Natural Science Foundation key project of Gansu Province (No. 24JRRA394), the National Natural Science Foundation of Gansu Province (No. 23JRRA1135), and the Fundamental Research Funds for the Central Universities (No. lzujbky-2023-pd06). We thank the Anhui Absorption Spectroscopy Analysis Instrument Co, Ltd. for XAFS measurements and analysis. We also appreciate Si-Min Yu from the Lanzhou Magnetic Resonance Center for her help with solid-state NMR characterization.

Declaration of competing interest

All the contributing authors report no conflict of interests in this work.

Author contribution statement

Y. C.: Data curation, project administration, validation, writing manuscript, experimental design. S. S. W.: Data curation, project administration, validation, experimental design. Y. Z.: Data curation, project administration, validation. H. Z. L.: Data curation, project administration, validation. J. M. Z.: Data curation, project administration, experimental design. N. Z.: Project administration, validation, experimental design. Y. T. Z.: Data curation, project administration, validation. Z. Y. H.: Data curation, project administration. L. A.: Project administration, funding acquisition, writing manuscript. P. X. X.: Project administration, funding acquisition, writing manuscript. All the authors have approved the final manuscript.

Use of AI statement

None.

References

[1] Li, X. D.; Wang, S. M.; Li, L.; Zu, X. L.; Sun, Y. F.; Xie, Y. Opportunity of atomically thin two-dimensional catalysts for promoting CO_2 electroreduction. *Acc. Chem. Res.* **2020**, *53*, 2964–2974.

[2] Chu, S.; Majumdar, A. Opportunities and challenges for a sustainable energy future. *Nature* **2012**, *488*, 294–303.

[3] Salvatore, D. A.; Gabardo, C. M.; Reyes, A.; O'Brien, C. P.; Holdcroft, S.; Pintauro, P.; Bahar, B.; Hickner, M.; Bae, C.; Sinton, D. et al. Designing anion exchange membranes for CO_2 electrolysers. *Nat. Energy* **2021**, *6*, 339–348.

[4] Gu, J.; Hsu, C. S.; Bai, L. C.; Chen, H. M.; Hu, X. L. Atomically dispersed Fe^{3+} sites catalyze efficient CO_2 electroreduction to CO. *Science* **2019**, *364*, 1091–1094.

[5] Kuhl, K. P.; Cave, E. R.; Abram, D. N.; Jaramillo, T. F. New insights into the electrochemical reduction of carbon dioxide on metallic copper surfaces. *Energy Environ. Sci.* **2012**, *5*, 7050–7059.

[6] Ross, M. B.; De Luna, P.; Li, Y. F.; Dinh, C. T.; Kim, D.; Yang, P. D.; Sargent, E. H. Designing materials for electrochemical carbon dioxide recycling. *Nat. Catal.* **2019**, *2*, 648–658.

[7] Caballero, A.; Pérez, P. J. Methane as raw material in synthetic chemistry: The final frontier. *Chem. Soc. Rev.* **2013**, *42*, 8809–8820.

[8] Hung, S. F.; Xu, A. N.; Wang, X.; Li, F. W.; Hsu, S. H.; Li, Y. H.; Wicks, J.; Cervantes, E. G.; Rasouli, A. S.; Li, Y. C. et al. A metal-supported single-atom catalytic site enables carbon dioxide hydrogenation. *Nat. Commun.* **2022**, *13*, 819.

[9] Wei, C.; Feng, Z. X.; Scherer, G. G.; Barber, J.; Shao-Horn, Y.; Xu, Z. J. Cations in octahedral sites: A descriptor for oxygen electrocatalysis on transition-metal spinels. *Adv. Mater.* **2017**, *29*, 1606800.

[10] Zhao, Q.; Yan, Z. H.; Chen, C. C.; Chen, J. Spinels: Controlled preparation, oxygen reduction/evolution reaction application, and beyond. *Chem. Rev.* **2017**, *117*, 10121–10211.

[11] Xie, W.; Ong, S. J. H.; Shen, Z. H.; Tian, L. Y.; Tang, K.; Xi, S. B.; Xu, Z. J. Critical role of tetrahedral coordination in determining the polysulfide conversion efficiency on spinel oxides. *J. Am. Chem. Soc.* **2025**, *147*, 988–997.

[12] Sun, Y. M.; Liao, H. B.; Wang, J. R.; Chen, B.; Sun, S. N.; Ong, S. J. H.; Xi, S. B.; Diao, C. Z.; Du, Y. H.; Wang, J. O. et al. Covalency competition dominates the water oxidation structure–activity relationship on spinel oxides. *Nat. Catal.* **2020**, *3*, 554–563.

[13] Zhang, T. T.; Yuan, B. W.; Wang, W. L.; He, J.; Xiang, X. Tailoring *H intermediate coverage on the $CuAl_2O_4$/CuO catalyst for enhanced electrocatalytic CO_2 reduction to ethanol. *Angew. Chem., Int. Ed.* **2023**, *62*, e202302096.

[14] Zhao, H. Y.; Zhu, L.; Yin, J.; Jin, J.; Du, X.; Tan, L.; Peng, Y.; Xi, P. X.; Yan, C. H. Stabilizing lattice oxygen through Mn doping in $NiCo_2O_{4-\delta}$ spinel electrocatalysts for efficient and durable acid oxygen evolution. *Angew. Chem., Int. Ed.* **2024**, *63*, e202402171.

[15] Xu, R. X.; Lan, X.; Jing, Y. L.; Niu, X. Y.; Zhao, L.; Hao, H. G. Mechanism of Ni-modified cecucoalo catalyst in promoting SO_2 tolerance for CO-SCR: Experimental and dft studies. *Fuel* **2025**, *390*, 134274.

[16] Chen, S. H.; Zheng, X. B.; Zhu, P.; Li, Y. P.; Zhuang, Z. C.; Wu, H. J.; Zhu, J. X.; Xiao, C. H.; Chen, M. Z.; Wang, P. S. et al. Copper atom pairs stabilize *OCCO dipole toward highly selective CO_2 electroreduction to C_2H_4. *Angew. Chem., Int. Ed.* **2024**, *63*, e202411591.

[17] Ma, F. Y.; Zhang, P. F.; Zheng, X. B.; Chen, L.; Li, Y. R.; Zhuang, Z. C.; Fan, Y. M.; Jiang, P.; Zhao, H.; Zhang, J. W. et al. Steering the site distance of atomic Cu–Cu pairs by first-shell halogen coordination boosts CO_2-to-C_2 selectivity. *Angew. Chem., Int. Ed.* **2024**, *63*, e202412785.

[18] Xu, Q. C.; Joensen, B. Ó.; Kani, N. C.; Sartori, A.; Willson, T.; Varcoe, J. R.; Riillo, L.; Ramunni, A.; Drnec, J.; Chorkendorff, I. et al. Electrolyte effects in membrane-electrode-assembly CO electrolysis. *Angew. Chem., Int. Ed.* **2025**, *64*, e202501505.

[19] Qiu, R. X.; Cui, L. X.; Peng, L.; Syzgantseva, O. A.; Li, J. R.; Fang, N.; Syzgantseva, M. A.; Jiang, Y.; Zhang, J.; Zhang, B. X. et al. Cooperative promotion of electroreduction of CO to *n*-propanol by *CO enrichment and proton regulation. *Chem. Sci.* **2025**, *16*, 8897–8909.

[20] Zhou, X. L.; Shan, J. Q.; Chen, L.; Xia, B. Y.; Ling, T.; Duan, J. J.; Jiao, Y.; Zheng, Y.; Qiao, S. Z. Stabilizing Cu^{2+} ions by solid solutions to promote CO_2 electroreduction to methane. *J. Am. Chem. Soc.* **2022**, *144*, 2079–2084.

[21] Wu, S. S.; Tian, M.; Hu, Y.; Zhang, N.; Shen, W.; Li, J. Y.; Guo, L. C.; Da, P. F.; Xi, P. X.; Yan, C. H. CeO_2 Promotes CO_2 electroreduction to formate on Bi_2S_3 via tuning of the *OCHO intermediate. *Inorg. Chem.* **2023**, *62*, 4088–4096.

[22] Wan, T. T.; Lv, C. M.; Ye, K.; Ma, M. C.; Hu, D.; Xiao, J. X.; Xiao, W. Stabilizing oxidation state of Cu via Ce doping into La_2CuO_4 for enhanced electroreduction of CO_2 to multicarbon products. *Small Methods*, in press, DOI: 10.1002/smtd.202500005.

[23] Guan, X. S.; Wang, X. K.; Zhang, X. C.; Zhang, C. M.; Chuang, S. S. C.; Li, Z. Boosting CO_2 fixation into dimethyl carbonate via multiple active sites constituted by $V_{O–Ce–O}$ vacancy clusters on single-unit-cell CeO_2 nano-sheets. *Angew. Chem., Int. Ed.*, in press, DOI: 10.1002/anie.202423958.

[24] Cheng, X. W.; Tu, Y.; Zhang, D. L.; Han, D.; Huang, L. C.; Hu, J.; Ding, H. H.; Xu, Q.; Zhu, J. F. CO adsorption, activation, and oxidation on CeO_2 (111)-supported Fe model catalyst surfaces. *Nano Res.* **2025**, *18*, 94907093.

[25] Liu, J.; Bao, H. L.; Zhang, B. S.; Hua, Q. F.; Shang, M. F.; Wang, J. Q.; Jiang, L. H. Geometric occupancy and oxidation state requirements of cations in cobalt oxides for oxygen reduction reaction. *ACS Appl. Mater. Interfaces* **2019**, *11*, 12525–12534.

[26] Wu, M.; Yang, R. O.; Duan, J. Y.; Zhu, S. C.; Chen, B. W.; Shi, Z. Y.; Liu, Y. W.; Li, H. Q.; Xia, B. Y.; Zhai, T. Y. Polymer-halogen pockets steering *CO adsorption configurations for highly selective CO_2 electroreduction. *Adv. Mater.* **2025**, *37*, 2504292.

[27] Carta, D.; Marras, C.; Loche, D.; Mountjoy, G.; Ahmed, S. I.; Corrias, A. An X-ray absorption spectroscopy study of the inversion degree in zinc ferrite nanocrystals dispersed on a highly porous silica aerogel matrix. *J. Chem. Phys.* **2013**, *138*, 054702.

[28] Tangcharoen, T.; Klysubun, W.; Kongmark, C. Synchrotron X-ray absorption spectroscopy and cation distribution studies of $NiAl_2O_4$, $CuAl_2O_4$, and $ZnAl_2O_4$ nanoparticles synthesized by sol–gel auto combustion method. *J. Mol. Struct.* **2019**, *1182*, 219–229.

[29] Dai, Z. C.; Chen, Y. X.; Zhang, H. K.; Cheng, M. Y.; Zhang, B. C.; Feng, P. Y.; Feng, Y. F.; Zhang, G. Q. Surface engineering on bulk Cu_2O for efficient electrosynthesis of urea. *Nat. Commun.* **2025**, *16*, 3271.

[30] Wei, Y. C.; Hu, Y.; Da, P. F.; Weng, Z.; Xi, P. X.; Yan, C. H. Triggered lattice-oxygen oxidation with active-site generation and self-termination of surface reconstruction during water oxidation. *Proc. Natl. Acad. Sci. USA* **2023**, *120*, e2312224120.

[31] Delmo, E. P.; Wang, Y. A.; Song, Y. H.; Zhu, S. Q.; Zhang, H. C.; Xu, H. M.; Li, T. H.; Jang, J.; Kwon, Y.; Wang, Y. N. et al. *In situ* infrared spectroscopic evidence of enhanced electrochemical CO_2 reduction and C–C coupling on oxide-derived copper. *J. Am. Chem. Soc.* **2024**, *146*, 1935–1945.

[32] Kuang, S. Y.; Su, Y. Q.; Li, M. L.; Liu, H.; Chuai, H.; Chen, X. Y.; Hensen, E. J. M.; Meyer, T. J.; Zhang, S.; Ma, X. B. Asymmetrical electrohydrogenation of CO_2 to ethanol with copper–gold heterojunctions. *Proc. Natl. Acad. Sci. USA* **2023**, *120*, e2214175120.